Composition of Organics on Asteroid (101955) Bennu

H. H. Kaplan[1], A. A. Simon[1], V. E. Hamilton[2], M. S. Thompson[3], S. A. Sandford[4], M. A. Barucci[5], E. A. Cloutis[6], J. Brucato[7], D. C. Reuter[1], D. P. Glavin[1], B. E. Clark[8], J. P. Dworkin[1], H. Campins[9], J. P. Emery[10], S. Fornasier[5,11], X. D. Zou[12], and D. S. Lauretta[13]

[1] NASA Goddard Space Flight Center, Greenbelt, MD, USA

[2] Southwest Research Institute, Boulder, CO, USA

[3] Department of Earth, Atmospheric, and Planetary Sciences, Purdue University, West Lafayette, IN, USA

[4] NASA Ames Research Center, Moffett Field, CA, USA

[5] LESIA, Observatoire de Paris, Université PSL, CNRS, Université de Paris, Sorbonne Université, 5 place Jules Janssen, 92195 Meudon, France

[6] Department of Geography, University of Winnipeg, Winnipeg, Canada

[7] INAF–Arcetri Astrophysical Observatory, Florence, Italy

[8] Department of Physics, Ithaca College, Ithaca, NY, USA

[9] Department of Physics, University of Central Florida, Orlando, Florida, USA

[10] Northern Arizona University, Flagstaff, AZ, USA

[11] Institut Universitaire de France (IUF), Paris, France

[12] Planetary Science Institute, Tucson, AZ, USA

[13] Lunar and Planetary Laboratory, University of Arizona, Tucson, AZ, USA

ABSTRACT

Context. The Origins, Spectral Interpretation, Resource Identification, and Security–Regolith Explorer (OSIRIS-REx) mission detected an infrared absorption at 3.4 μm on near-Earth asteroid (101955) Bennu. This absorption is indicative of carbon species, including organics, on the surface.

Aims. We aim to describe the composition of the organic matter on Bennu by investigating the spectral features in detail.

Methods. We use a curated set of spectra acquired by the OSIRIS-REx Visible and InfraRed Spectrometer (OVIRS) that have features near 3.4 μm (3.2 to 3.6 μm) attributed to organics. We assess the shapes and strengths of these absorptions in the context of laboratory spectra of extraterrestrial organics and analogs.

Results. We find spectral evidence of aromatic and aliphatic CH bonds. The absorptions are broadly consistent in shape and depth with those associated with insoluble organic matter in meteorites. Given the thermal and space weathering environments on Bennu, it is likely that the organics have not been exposed for long enough to substantially decrease the H/C and destroy all aliphatic molecules.

Key words. minor planets, asteroids: individual: (101955) Bennu / techniques: spectroscopic / planets and satellites: composition

1. Introduction

The Origins, Spectral Interpretation, Resource Identification, and Security–Regolith Explorer (OSIRIS-REx) mission detected carbon species including organics and carbonates on near-Earth asteroid (101955) Bennu (Kaplan et al. 2020; Simon et al. 2020b). These findings, based on the presence of an infrared absorption near 3.4 μm, indicate that the sample of Bennu's regolith that the OSIRIS-REx spacecraft will return to Earth in 2023 (Lauretta et al. 2021, 2017) is likely to contain carbon-bearing material. The organic component may hold clues to the conditions of the early solar system and the origins of life on Earth (e.g., Chyba et al. 1990).

Bennu has been spectrally linked to aqueously altered CI- and CM-type carbonaceous chondrites (Clark et al. 2011; Hamilton et al. 2019); these primitive carbon-rich meteorites are likely the closest analogs of Bennu currently available for laboratory studies. CI and CM chondrites contain 1 to 5 wt.% total carbon in organic and inorganic forms (Pearson et al. 2006; Alexander et al. 2012; Sephton 2002). The majority of the meteoritic carbon (>70 wt.%) is hosted in insoluble organic matter (IOM), an acid-insoluble, kerogen-like macromolecule that is structurally complex with variable isotopic and elemental composition (Cody & Alexander 2005; Alexander et al. 2017). The soluble organic matter (SOM) represents a much smaller fraction (up to 0.1%) of the total carbon, with the remainder of carbon either unaccounted for with current techniques or contained in inorganic forms (e.g., carbonates, nanodiamonds). Meteoritic SOM can be highly complex with a variety of different compound classes such as amino acids, carboxylic acids, hydroxy acids, amines, alcohols, aldehydes, ketones, N-heterocycles, polyols, aliphatic and aromatic hydrocarbons, and sugars (e.g., Glavin et al. 2018).

Most of the meteoritic organic matter likely originated in the interstellar medium or in the colder regions of the protoplanetary disk before being incorporated into the earliest solar system bodies. Such bodies include the parent asteroids of the carbonaceous chondrites and of Bennu, which is the rubble-pile descendant of a larger body that was catastrophically disrupted (e.g., Barnouin et al. 2019; Michel et al. 2020). Differences in the organic abundances, distributions, and isotopic and elemental compositions within and between carbonaceous chondrite groups have been attributed to nebular processes, thermal and/or aqueous alteration of the parent body (e.g., Herd et al. 2011;

Alexander et al. 2007; Glavin et al. 2010), and surface modification such as space weathering (e.g., Thompson et al. 2020).

2. Observations and Methods

The OSIRIS-REx Visible and InfraRed Spectrometer (OVIRS) (Reuter et al. 2018) has a circular, 4 mrad field of view. It collected tens of thousands of spectra of Bennu with wavelengths from 0.4 to 4.3 μm. In the wavelength region near 3.4 μm (3.2 to 3.6 μm), there are at least four absorptions characteristic of organic carbon, resulting from the symmetric and asymmetric stretching modes of methyl (-CH_3) and methylene (-CH_2) groups (i.e., aliphatic CH) (e.g., Allen & Wickramasinghe 1981; Pendleton 1995).

We analyzed spectra collected during the sample site reconnaissance (Recon A) phase of the OSIRIS-REx mission in October 2019 (Lauretta et al. 2021, 2017). The Recon A dataset in this study comprises 15,585 photometrically corrected OVIRS spectra that cover 10% of the surface, focused on regions of interest including the Nightingale site (Hokioi crater) where OSIRIS-REx collected its sample (see Appendix A for more observation details and coverage map). We used these data, rather than the global-coverage dataset at 20 m per footprint (Simon et al. 2020b), because the spatial resolution (4-5 m cross-track and 7-10 m along-track) is optimized to isolate organic-rich regions of the surface.

We used laboratory spectra to directly compare the OVIRS spectra from 2.9 to 3.6 μm with well-studied organic endmembers. Laboratory spectra included in our analyses are of IOM extracted from carbonaceous chondrites; material captured from comet 81P/Wild 2 by the Stardust spacecraft, which may have been modified by the capture process, though the spectrum resembles spectra of primitive interplanetary dust particles (Keller et al. 2006); a laboratory-made, irradiated ice tholin, which was created to approximate cometary organic matter (Khare et al. 1993); and terrestrial asphaltite (Moroz et al. 1998) (Fig. 1c, Fig. 2, Table A.1). These laboratory endmembers are chosen as the most likely organic components to be observed at the macro-scale on Bennu based on meteorite analyses and previous observations (Simon et al. 2020b). We also include a set of ammonium salt spectra with our laboratory endmembers to distinguish nitrogen-bearing phases, which may be present on comets and some asteroids, and have absorptions in the wavelength range (2.9 – 3.6 μm) studied here (Poch et al. 2020).

We used linear least-squares and Kolmogorov-Smirnov goodness-of-fit methods to determine the closest matches between OVIRS spectra and laboratory spectra with respect to spectral shape (see Appendix A). The same least-squares comparison method was previously used to identify carbonate-rich spots on Bennu by identifying 3.4 μm features with a doublet spectral shape and band positions indicative of carbonates rather than organics; we find that least-squares fits with χ^2 values < 2 provide credible matches to the OVIRS data (Kaplan et al. 2020). The Kolmogorov-Smirnov method was subsequently used to confirm these results (Ferrone et al. 2021, see Appendix A).

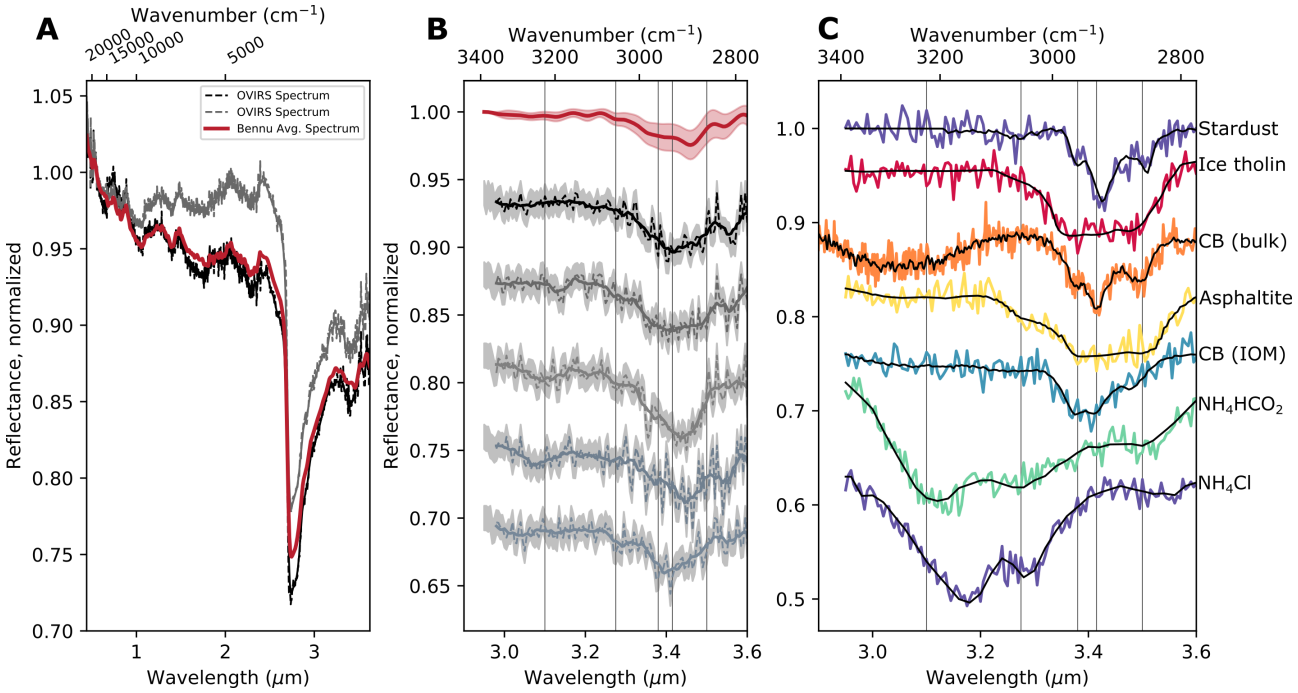

Fig. 1. Evidence of organics on Bennu in spectral features near 3.4 μm. a) Average OVIRS spectrum of Bennu (red) and two OVIRS spectra of Bennu with spectral features near 3.4 μm. (b) Close-up of the continuum-removed region around 3.4 μm, offset, with wavelengths of C-H absorptions indicated by vertical gray lines. Top three spectra are the same as shown in panel a. Shaded region indicates uncertainties and vertical lines at 3.10, 3.275, 3.38, 3.42, and 3.50 μm indicate positions of possible absorption features. (c) Laboratory spectra near 3.4 μm for comparison. Black lines are the spectra and colors are spectra with noise-added to simulate OVIRS noise. CB is Cold Bokkeveld; bulk refers to the whole meteorite; and IOM refers to the extracted, insoluble organic component.

Finally, we measured the strength of the CH absorption feature from the continuum at 3.42 μm (i.e., band depth at 3.42 μm; Clark & Roush 1984) as another method for assessing organic composition (H/C) and concentration (C wt.%). Band depth at 3.42 μm has been linked to the composition and concentration of organic matter in sedimentary rocks and meteorites (e.g., Herron et al. 2014; Kaplan & Milliken 2018). For IOM extracted from carbonaceous chondrites, band depth is positively correlated with the hydrogen-to-carbon ratio (H/C) (Kaplan et al. 2019). If there is not enough hydrogen in the organics (i.e., H/C < 0.3), there will be no absorption at 3.42 μm. For IOM in bulk rock (i.e., meteorites), the absolute concentration is also important: >1 wt.% C is needed to observe an absorption at 3.42 μm (Kaplan et al. 2019). Most CMs and CIs contain 1–3 wt.% C and have bulk H/C ratios in the IOM > 0.5 (Alexander et al. 2007).

3. Results

3.1. Spectral Features

Most OVIRS spectra appear to be a mixture of organic and carbonate material, which are not suitable for our analysis. In total, only 237 of the 15,585 spectra analyzed are well fit by the organic laboratory spectra described in Section 2 ($\chi^2 < 2$) (see Appendix A). We refer to these hereafter as organic-rich spectra because they have absorption band positions and widths that match laboratory organic spectra (Fig. 1). These organic-rich spectra are distributed across the asteroid surface (i.e.,

are not concentrated in any given region), suggesting a wide spatial distribution of organics (Ferrone et al. 2021). The spectral features themselves are not homogenous and have varying absorption strengths and shapes (Simon et al. 2020b).

The organic-rich spectra typically have a strong absorption at 3.42 μm, which is consistent with the position of the symmetric $–CH_2$ stretch (Fig. 1b). The entire absorption spans from 3.2 to 3.5 μm, covering the full set of aliphatic CH stretches. The surface-averaged OVIRS spectrum (Fig. 1a,b, red spectrum) has a minimum at 3.47 μm that likely reflects the contribution from carbonates. The asymmetric CH stretches (3.38 or 3.42 μm) are typically stronger than their longer wavelength (lower wavenumber) symmetric counterparts, so spectra dominated by aliphatic organics should not have the strongest feature at 3.47 μm. Although there does appear to be some structure within this region, the most identified absorptions (3.38, 3.42, 3.47, 3.5 μm) are not as well-resolved in the OVIRS spectra as they are in some laboratory spectra (e.g., Cold Bokkeveld CM chondrite, Fig. 1). The signal-to-noise ratio (SNR) and spectral resolution for the OVIRS data in this region are both lower than that of the laboratory spectra, which likely accounts for the inability to resolve the individual organic absorptions (see Fig. A.2, Appendix A, and Reuter et al. (2018)); laboratory spectra with noise added to achieve SNR of the OVIRS spectra are shown in Figures 1 and 2 (see Appendix A).

Some of the OVIRS organic-rich spectra appear to have a “shoulder” or weak absorption near 3.3 μm that is consistent with aromatic CH stretch (Figs. 1b, A.3). Although this spectral feature is common in some pure, laboratory organics, it is uncommon in bulk meteorite spectra owing to stronger, overlapping hydration features and low absorption cross-section (Dartois et al. 2004; Kaplan et al. 2019). A strong absorption band at 3.3 μm has, however, been observed on comet 67P/Churyumov-Gerasimenko (67P) by the Rosetta mission, suggesting the presence of polycyclic aromatic hydrocarbons with free aromatic CH stretching (Raponi et al. 2020). An alternative explanation of the 3.3-μm band on 67P, along with an absorption at 3.1 μm, is due to N-H vibration modes from the presence of ammonia salts (Poch et al. 2020). Some OVIRS spectra of Bennu do appear to have a weak feature at 3.1 μm that is consistent with some NH-bearing phases (Fig. 1a, 2c,A.3)

Outside of the 2.9 to 3.6 μm wavelength region, the organic-rich spectra are broadly similar to the average VNIR spectrum of Bennu, which has a hydration feature at 2.74 μm, suggesting that the surface composition is dominated by Mg-rich phyllosilicates (Hamilton et al. 2019) (Fig. 1a). There are also a series of minor absorption features at shorter wavelengths (<2.5 μm) that are related to the hydrated phyllosilicates and iron oxides (Simon et al. 2020a). We do not find a correlation between any phyllosilicate spectral features and organic features in the Recon A spectra, consistent with the coarser-scale global OVIRS observations (Simon et al. 2020b).

3.2. Organic H and C Abundances

In terms of overall spectral shape, IOM extracted from the carbonaceous chondrite meteorites are the best fit to all organic-rich OVIRS spectra (Figure 2). We find some examples (Figure 2b) where there may be additional absorption features not seen in the IOM spectra, but the feature at 3.2 – 3.6 μm is still the dominant absorption and IOM provides the best spectral match of any laboratory endmember. The 18 IOM laboratory spectra used as laboratory spectral endmembers have similar spectral shapes with small differences in methyl and methylene absorption strengths (3.38 μm vs. 3.42 μm band depth) resulting from different aliphatic chain length (e.g., Orthous-Daunay et al. 2013; Kebukawa et al. 2011). Using the linear least-squares and Kolomorgov-Smirnov fitting techniques we can distinguish IOM spectral shapes from other organics and carbonates in data with SNR of the OVIRS data with high confidence (Table A.2) but differentiating between IOM from individual meteorites is more difficult (Table A.3). Therefore, we group spectral fits as generally IOM-like.

The carbonaceous chondrites and IOM provide constraints on the elemental composition of Bennu's organics. The presence of an aliphatic spectral feature in IOM indicates that the H/C ratio is greater than 0.3 (Kaplan et al. 2019), suggesting that the minimum H/C on Bennu is 0.3. Using band depth at 3.42 μm to estimate H/C from the spectrum, we find H/C values ranging from 0.4 to 0.6 for Bennu's organic-rich spectra identified in this study (Figure 3a). Given that the contribution from carbonate in the spectral region near 3.4 μm is unknown (Kaplan et al., 2020) and the contribution of organic abundance to 3.42 μm band depth (Kaplan et al. 2019), these values are upper limits. The high end of this range is typical of the CM and CI chondrites (Figure 3a), which are Bennu's closest analogs (Hamilton et al. 2019, 2021).

Estimates of organic abundance on Bennu are greatly complicated by the presence of carbonates, which have overlapping spectral features at 3.4 μm (Kaplan et al. 2020). In addition, organic spectral models for assessing abundance can be strongly affected by organic composition, making it difficult to determine exact abundances, as has been shown for Ceres (Kaplan et al. 2018). That said, the 3.42 μm band depths observed in the OVIRS spectra studied here are consistent with carbonaceous chondrites that contain 1 – 2.5 wt.% C (Fig. 3b), suggesting that similar concentrations of organics could be present on Bennu. The organic-rich regions of Ceres, on the other hand, have a stronger absorption feature at 3.4 μm than any carbonaceous chondrite. This strong feature has been used as evidence of an endogenous mechanism for further concentrating organic matter beyond what was originally incorporated into the body (De Sanctis et al. 2019, 2017; Kaplan et al. 2018; Marchi et al. 2019), a mechanism which is neither likely in Bennu's case nor needed to explain the spectra.

The 3.42 μm band depth reflects the combination of organic composition (e.g., H/C) and abundance (e.g., C wt.%) in bulk meteorites (Figure 3c). If we assume there is 2.5 wt.% C on Bennu, then the range in 3.42 μm band depth for the organic-rich spectra is consistent with H/C of 0.3 to 0.6; smaller C abundances would require high H/C values. To untangle these values will require

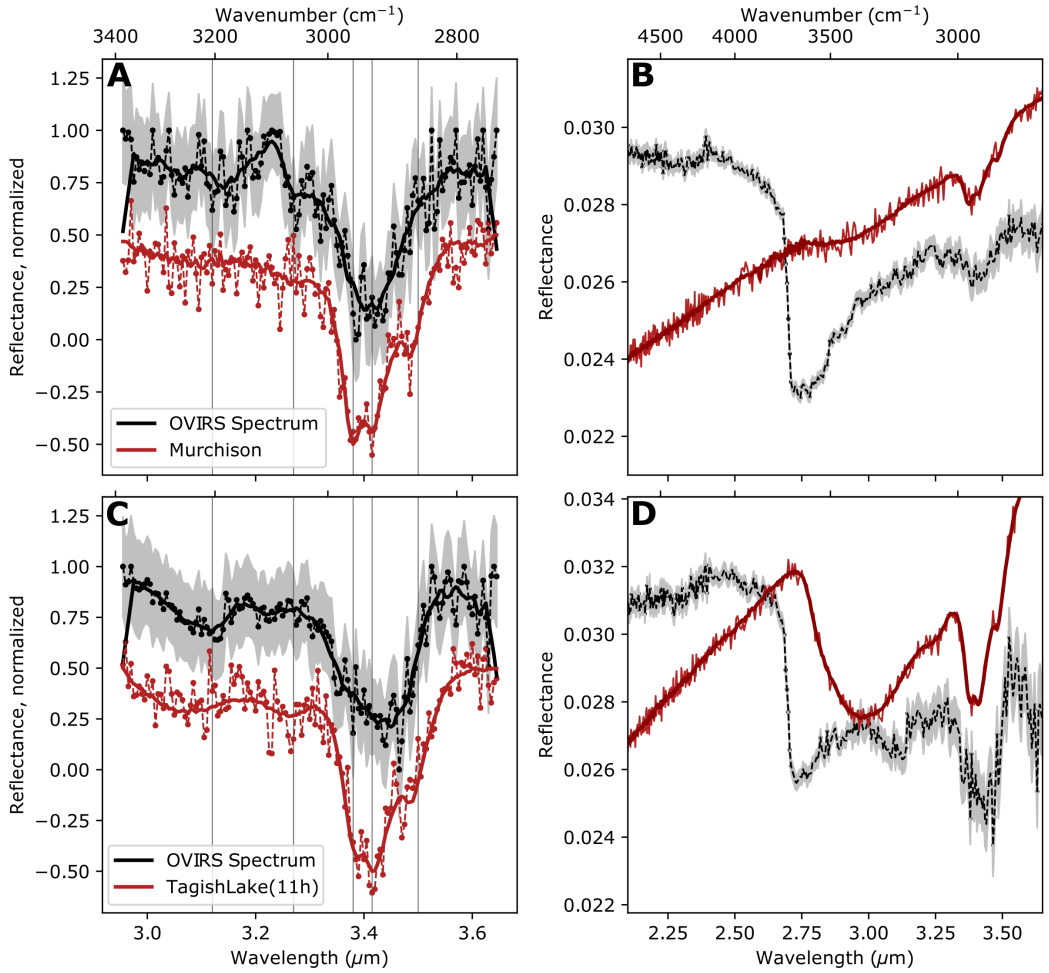

Fig. 2. Laboratory spectral matches for organic spectral shapes observed on Bennu. Most common spectral shapes in the Bennu spectra that we analyzed are well-matched with spectra of meteorite IOM. (a and c) Best fits in the 3.1 to 3.6 μm region between OVIRS spectra (black) and IOM spectra (red, solid) with noised added to simulate OVIRS noise (red, dashed); spectra are normalized from 0 to 1 and offset for clarity. Shaded region indicates uncertainties and vertical lines at 3.10, 3.275, 3.38, 3.42, and 3.50 μm indicate positions of possible absorption features. (b and d) OVIRS and IOM spectra from 2.1 to 3.6 μm shown without normalization or continuum removal; IOM spectra have been scaled.

additional laboratory measurements of the returned samples. However, the range of H and C values suggested by Bennu's 3.4 μm absorption feature are broadly consistent with the carbonaceous chondrites and fall in the same range as available CM chondrite spectra.

Absorption features due to C-C, C=C, and C=O bonds result from aromatic structures, ketones, and carboxyls that are prominent in meteorite IOM; however, they are absent in the wavelength range covered by OVIRS spectra (0.4 to 4.3 μm). Therefore, we expect there to be an additional, unknown amount of carbon in aromatic structures, reduced compounds (nanodiamond, graphite, and carbides), or amorphous material that is not detectable with OVIRS and cannot be quantified from our observations, but will be determined from the returned sample.

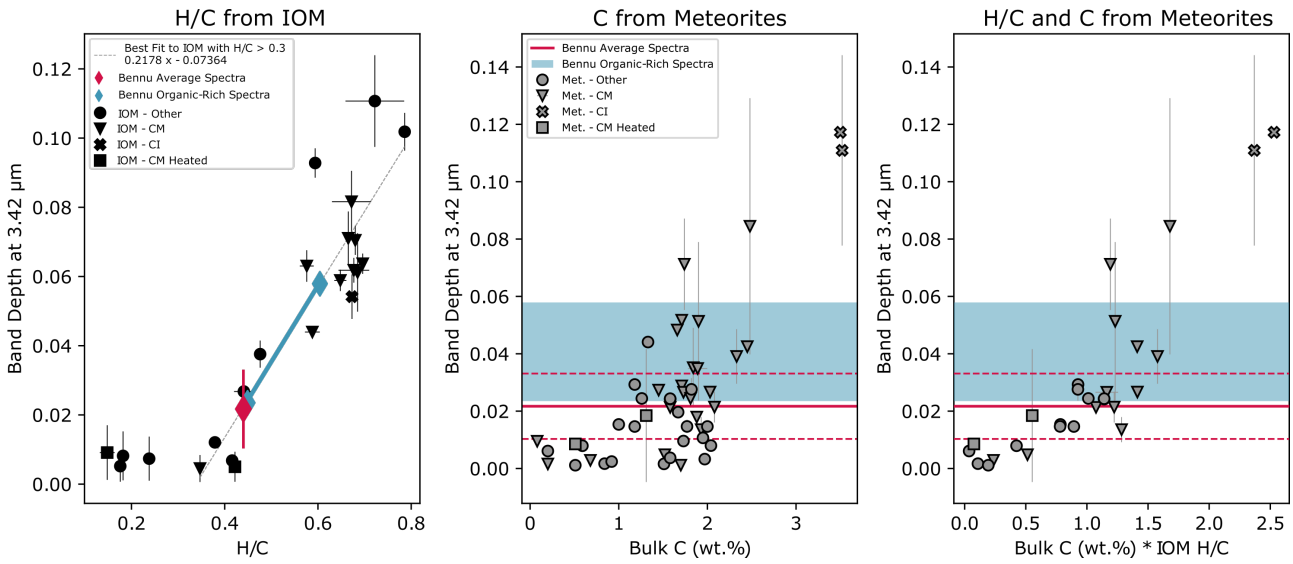

Fig. 3. Estimated H/C. (a) Carbonaceous chondrite IOM band depth at 3.42 µm, plotted against H/C (atom.) from Alexander et al. (2007); "other" refers to IOM from CV, CO, CR, and ungrouped carbonaceous chondrites. The 3.42 µm band depths from OVIRS Recon A average (red diamond) and organic-rich spectra (blue diamonds) are plotted on the IOM trend to estimate the upper limit on H/C of 0.6 for Bennu. (b) Carbonaceous chondrite (i.e., bulk meteorite) band depth at 3.42 µm plotted against wt.% C for those meteorites (symbology is the same as in panel a but for bulk meteorites as opposed to IOM; grey triangle, CM-type; grey cross, CI-type; grey square, heated CM-type; grey circle, other carbonaceous chondrite IOM including CV, CO, CR, and ungrouped). Band depth at 3.42 µm is also shown for OVIRS organic-rich (blue shaded region) and Bennu global average spectra (red solid line; standard deviation, red dashed lines). The Bennu organic-rich spectra have similar band depths to carbonaceous chondrites containing 1 – 2.5 wt.% C. (c) a combination of wt.% C and H/C of IOM is the best predictor of 3.42 µm band depth in the meteorites.

4. Discussion

The spectral features from 2.9 to 3.6 µm observed on the Bennu allow us to compare this asteroid to other extraterrestrial settings. The OVIRS data are comparable to the spectra seen in the diffuse interstellar medium (Allen & Wickramasinghe 1981; Sandford et al. 1991), comet 67P (Raponi et al. 2020), and multiple large main-belt asteroids (Simon et al. 2020b). We find that carbonaceous chondrite IOM is the closest laboratory analog to Bennu's organics based on the available spectral data at the wavelengths covered by the OVIRS instrument. This finding strengthens the previously described connection between Bennu and carbonaceous chondrite meteorites (Clark et al. 2011; Hamilton et al. 2019, 2021). The macro-scale heterogeneity of organic-rich spectra of Bennu has not been observed elsewhere in the solar system (potentially owing to a lack of spacecraft data in most cases) but is mirrored in the large heterogeneity seen at small scales in meteorite organics (e.g., Alexander et al. 2017).

The organics on Bennu may reflect heterogenous aqueous alteration conditions. Although aqueous alteration has been reported to decrease H/C (Herd et al. 2011),), modification of organics is primarily controlled by heating (Alexander et al. 2014; Quirico et al. 2018) and variation in H/C and C wt.% estimated for organic-rich OVIRS spectra may be the result of variable heating (Figure 3). Typically, higher H/C values are also associated with higher N/C, O/C, and bulk C (Alexander et al. 2007). Though spectra with a feature near 3.1 µm may indicate the presence or increased

abundance of nitrogen-bearing phases, the absorption is weak, and more work is needed to understand the possibility of these phases on Bennu.

However, outside of the 3.4 μm region, Bennu is spectrally similar to CI and CM carbonaceous chondrites of petrographic subtypes < 2.4, based on the Rubin et al. (2007) scale, including some that are mildly heated (Hamilton et al. 2019, 2021; Kaplan et al. 2020); other indications of aqueous alteration, such as 2.7 μm hydration band depth, do not correspond to the organic variation.

Bennu's surface has been exposed to high temperatures during its 1.75 million years in near-Earth space (Ballouz et al. 2020). It has also been exposed to weathering in the space environment for as many as 50 million to 1 billion years, based on maximum crater retention ages (Walsh et al. 2019); Bierhaus et al. in prep). Temperature and solar wind irradiation break down aliphatic organics by removing hydrogen (Kebukawa et al. 2010; Laczniak et al. 2021), weakening or erasing the aliphatic absorption feature at 3.4 μm. Kebukawa et al. (2010) used Murchison IOM (one of the laboratory organic analogs used in this study) to determine that aliphatic CH is lost within 200 years at 100ºC (373K). Bennu's maximum surface temperatures exceed this temperature for multiple hours each day at perihelion for much of the surface (Rozitis et al. 2020), which would lead to destruction of aliphatic organics over Bennu's near-Earth lifetime. However, small-scale surface roughness allows for some regions (meter-scale or smaller) that continuously maintain maximum temperatures <0ºC (273 K) necessary to extend aliphatic organic lifetime to 100 million years (Rozitis et al. 2020; Kebukawa et al. 2010), and small-scale surface temperature heterogeneity could lead to the observed differences in organic band depth and spectral shape (Figure 2, 3).

Laboratory experiments have also shown diverging effects on the spectral trends and organic chemistry resulting from various constituent space weathering processes. Experiments simulating micrometeoroid bombardment of carbonaceous chondrites have shown an increase in detectable organics correlated with darkening and mild bluing slopes (Thompson et al. 2020). In contrast, studies simulating solar wind irradiation have shown reddening of the spectral slope correlated with a mixed efficiency for organic species destruction. Irradiation with 1 keV H+ ions resulted in only limited, if any, destruction of organics and mild spectral reddening, whereas 4 keV He+ irradiation resulted in strong reddening and a reduction in detectable organics by up to 40% over 10,000-year timescales (Laczniak et al. 2021). Thus, space weathering of organics may result in competitive spectral trends depending on the dominant constituent processes, initial composition, and/or the timescales of surface exposure.

The potential for rapid breakdown of aliphatic organics would indicate that where these compounds are observed on Bennu, the surface has been exposed for a relatively short period of time. Spectrophotometric studies suggest that Bennu's small craters may be less than tens of thousands of years old (DellaGiustina et al. 2020). In addition, evidence of particle ejection and re-impact (Lauretta et al. 2019) and thermally driven fracturing (Molaro et al. 2020) on Bennu indicates that ongoing surface processes are continually exposing fresh material at the surface.

5. Conclusions

The detection of organic matter on asteroid Bennu using the OVIRS instrument onboard the OSIRIS-REx spacecraft provides a preview of the composition of the sample that will be returned to Earth in 2023. Spectral features near 3.4 μm, including a strong absorption minimum between 3.38 and 3.42 μm and a possible shoulder at 3.3 μm, are indicative of aliphatic and aromatic CH with a maximum H/C of 0.6 and a minimum H/C of 0.3. The overall spectral shape in the OVIRS data is most comparable to meteorite IOM as opposed to other organic analogs. Elevated temperatures and space weathering should quickly alter these absorption features, so the strongest organic spectral features likely indicate the organic material relatively recently exposed by ongoing mass shedding and impact processes, and/or material that has been shielded from relatively high temperatures. The sample of Bennu's regolith returned by OSIRIS-REx will tell us about organic chemistry on Bennu beyond the CH-bearing material, particularly the detailed composition and structure of the IOM as well as details about the soluble organic diversity and composition.

Acknowledgements. We are grateful to the entire OSIRIS-REx Team for making the encounter with Bennu possible. This material is based upon work supported by NASA under Contract NNM10AA11C issued through the New Frontiers Program. OVIRS spectral data from Recon A are available via the Planetary Data System at https://sbn.psi.edu/pds/resource/orex/ovirs.html (Reuter et al. 2019). Data are delivered to the PDS according to the schedule in the OSIRIS-REx Data Management Plan, available in the OSIRIS-REx mission bundle at https://sbnarchive.psi.edu/pds4/orex/orex.mission/document/.

References

Alexander, C., Cody, G., De Gregorio, B., Nittler, L., & Stroud, R. 2017, Chemie der Erde - Geochemistry, 77, 227

Alexander, C. M. O., Bowden, R., Fogel, M. L., et al. 2012, Science, 337, 721

Alexander, C. M. O., Cody, G. D., Kebukawa, Y., et al. 2014, Meteoritics & Planetary Science, 49, 503

Alexander, C. M. O., Fogel, M., Yabuta, H., & Cody, G. 2007, Geochimica et Cosmochimica Acta, 71, 4380

Allen, D. A. & Wickramasinghe, D. T. 1981, Nature, 294, 239

Ballouz, R.-L., Walsh, K. J., Barnouin, O. S., et al. 2020, Nature, 587, 205

Barnouin, O. S., Daly, M. G., Palmer, E. E., et al. 2019, Nature Geoscience, 12, 247

Chyba, C., Thomas, P., Brookshaw, L., & Sagan, C. 1990, Science, 249, 366

Clark, B. E., Binzel, R. P., Howell, E. S., et al. 2011, Icarus, 216, 462

Clark, R. N. & Roush, T. L. 1984, Journal of Geophysical Research, 89, 6329

Cody, G. D. & Alexander, C. M. 2005, Geochimica et Cosmochimica Acta, 69, 1085

Dartois, E., Muñoz Caro, G. M., Deboffle, D., & d'Hendecourt, L. 2004, Astronomy & Astrophysics, 423, L33

De Sanctis, M. C., Ammannito, E., McSween, H. Y., et al. 2017, Science, 355, 719

De Sanctis, M. C., Vinogradoff, V., Raponi, A., et al. 2019, Monthly Notices of the Royal Astronomical Society, 482, 2407

DellaGiustina, D. N., Burke, K. N., Walsh, K. J., et al. 2020, Science, eabc3660

Ferrone, S., Clark, B., Kaplan, H., et al. 2021, Icarus, 114579, publisher: Elsevier

Glavin, D. P., Alexander, C. M., Aponte, J. C., et al. 2018, in Primitive Meteorites and Asteroids (Elsevier), 205–271

Glavin, D. P., Callahan, M. P., Dworkin, J. P., & Elsila, J. E. 2010, Meteoritics & Planetary Science, 45, 1948

Hamilton, V. E., Christensen, P. R., Kaplan, H. H., et al. 2021, Astronomy & Astrophysics, 650, A120

Hamilton, V. E., Simon, A. A., Christensen, P. R., et al. 2019, Nature Astronomy, 3, 332

Herd, C. D. K., Blinova, A., Simkus, D. N., et al. 2011, Science, 332, 1304

Herron, M., Loan, M., Charsky, A., et al. 2014, Petrophysics, 55, 434

Kaplan, H. H., Lauretta, D. S., Simon, A. A., et al. 2020, Science, 370, eabc3557

Kaplan, H. H. & Milliken, R. E. 2018, Clays and Clay Minerals

Kaplan, H. H., Milliken, R. E., & Alexander, C. M. O. 2018, Geophysical Research Letters, 45, 5274

Kaplan, H. H., Milliken, R. E., Alexander, C. M. O., & Herd, C. D. K. 2019, Meteoritics & Planetary Science

Kebukawa, Y., Alexander, C. M., & Cody, G. D. 2011, Geochimica et Cosmochimica Acta, 75, 3530

Kebukawa, Y., Nakashima, S., & Zolensky, M. E. 2010, Meteoritics & Planetary Science, 45, 99

Keller, L. P., Bajt, S., Baratta, G. A., et al. 2006, Science, 314, 1728

Khare, B., Thompson, W., Cheng, L., et al. 1993, Icarus, 103, 290

Laczniak, D., Thompson, M., Christoffersen, R., et al. 2021, Icarus, 114479

Lauretta, D. S., Balram-Knutson, S. S., Beshore, E., et al. 2017, Space Science Reviews, 212, 925

Lauretta, D. S., Enos, H. L., Polit, A. T., Roper, H. L., & Wolner, C. W. V. 2021, in Sample Return Missions, ed. A. Longobardo (Elsevier), 163–194

Lauretta, D. S., Hergenrother, C. W., Chesley, S. R., et al. 2019, Science, 366, eaay3544

Marchi, S., Raponi, A., Prettyman, T. H., et al. 2019, Nature Astronomy, 3, 140

Michel, P., Ballouz, R.-L., Barnouin, O. S., et al. 2020, Nature Communications, 11, 2655

Molaro, J. L., Hergenrother, C. W., Chesley, S. R., et al. 2020, Journal of Geophysical Research: Planets, 125, e2019JE006325, publisher: John Wiley & Sons, Ltd

Moroz, L., Arnold, G., Korochantsev, A., & Wäsch, R. 1998, Icarus, 134, 253

Orthous-Daunay, F.-R., Quirico, E., Beck, P., et al. 2013, Icarus, 223, 534

Pearson, V. K., Sephton, M. A., Franchi, I. A., Gibson, J. M., & Gilmour, I. 2006, Meteoritics & Planetary Science, 41, 1899

Pendleton, Y. J. 1995, Planetary and Space Science, 43, 1359

Poch, O., Istiqomah, I., Quirico, E., et al. 2020, Science, 367, eaaw7462

Quirico, E., Bonal, L., Beck, P., et al. 2018, Geochimica et Cosmochimica Acta, 241, 17

Raponi, A., Ciarniello, M., Capaccioni, F., et al. 2020, Nature Astronomy, 4, 500

Reuter, D. C., Simon, A. A., Hair, J., et al. 2018, Space Science Reviews, 214

Reuter, D. C., Simon, A. A., Lunsford, A., & Lauretta, D. S. 2019

Rozitis, B., Emery, J. P., Siegler, M. A., et al. 2020, Journal of Geophysical Research: Planets, 125

Rubin, A. E., Trigo-Rodríguez, J. M., Huber, H., & Wasson, J. T. 2007, Geochimica et Cosmochimica Acta, 71, 2361

Sandford, S. A., Allamandola, L. J., Tielens, A. G. G. M., et al. 1991, The Astrophysical Journal, 371, 607

Sephton, M. A. 2002, Natural Product Reports, 19, 292, publisher: The Royal Society of Chemistry

Simon, A., Reuter, D., Gorius, N., et al. 2018, Remote Sensing, 10, 1486

Simon, A. A., Kaplan, H. H., Cloutis, E., et al. 2020a, Astronomy & Astrophysics, 644, A148

Simon, A. A., Kaplan, H. H., Hamilton, V. E., et al. 2020b, Science, 370, eabc3522

Thompson, M., Morris, R. V., Clemett, S. J., et al. 2020, Icarus, 346, 113775

Walsh, K. J., Jawin, E. R., Ballouz, R.-L., et al. 2019, Nature Geoscience, 12, 242

Zou, X.-D., Li, J.-Y., Clark, B. E., et al. 2021, Icarus, 358, 114183

Appendix A: Supplementary Material

Appendix A.1: Additional Information on the Dataset

We used OVIRS spectra from the Recon A phase of the OSIRIS-REx mission, specifically, those that were collected on four separate dates in October 2019 (Reuter et al. 2019). These observations covered the mission's primary sample collection site, Nightingale, and three other candidate sample sites (Lauretta et al. 2021), as well as a few other areas of interest that were observed by opportunity. The spacecraft scanned the surface from a 1 km range with varying phase angles, with scan patterns shown in Fig. A.1. OVIRS data collected during Recon A have a spatial resolution of 4 to 5 m cross-track and 7 to 10 m along-track (36 m^2).

Appendix A.2: Methods: Calibration and Data Processing

Full details of the calibration pipeline are described in Simon et al. (2018). Briefly, each OVIRS spectrum comprises five segments collected from separate linear variable filters with overlapping wavelengths that are resampled to create a continuous spectrum from 0.39 to 4.3 μm (Reuter et al. 2018). A thermal tail is subtracted from calibrated radiance (resampled) spectra and the result is divided by solar flux to obtain reflectance (I/F) (Simon et al. 2020b). Thermal fill-in can occur when thermal emission at high temperatures leads to thermal flux within the band causing absorption features to appear weak. However, there is no indication that the 3.4-μm feature in OVIRS spectra collected during Recon is affected by thermal fill-in (Simon et al. 2020b).

To remove confounding effects of viewing geometry, we used the photometric model developed by Zou et al. (2021) to correct the OVIRS data to standard viewing geometry (incidence 30º, emission 0º, phase 30º). However, this photometric correction has insignificant effect at the wavelengths of interest in this study (e.g., 2.8 – 3.6 μm) and analyses with and without this correction are very similar.

A combination of warm surface temperatures and instrument temperatures led to decreasing SNR at the longest OVIRS wavelengths, including within the wavelength region of interest (Fig. A.2). A detailed discussion of the wavelength-dependent signal-to-noise ratio (SNR) for these OVIRS observations and its influence on spectral detection of organics or carbonates on Bennu using the 3.4 μm region can be found in Kaplan et al. (2020) and Simon et al. (2020b). Briefly, the Bennu SNR for Recon A was found by calculating the fractional RMS of calibrator spectra, inverting, and scaling that SNR value by ratio of the average radiance of an internal source to a representative Bennu spectrum for each observation date.

Appendix A.3: Methods: Organic Spectral Detection and Analysis

We followed methods outlined in Simon et al. (2020b) and Kaplan et al. (2020) to perform our organic spectral analysis. Specifically, we used a three-point quadratic polynomial to fit to each OVIRS spectrum at 2.9, 3.2, and 3.6 μm to approximate the spectral continuum. We divided out this

continuum and performed further analyses on the continuum-removed dataset. We calculated band depths by taking an average of three channels surrounding the wavelength of interest and calculated the depth relative to the continuum reflectance. A set of laboratory spectra were resampled to OVIRS channels and treated in the same way for the sake of direct comparison (Table A.2, A.3). These spectra are all previously published, and references can be found in the main text. To compare spectral shape rather than feature strength, we normalized each continuum-removed spectrum to have a maximum value of 1 and minimum value of 0 (Figure 2). All analyses were performed on unsmoothed spacecraft data and reflect the noise inherent in spacecraft data; Figure 1 and 2 also show spectra smoothed to demonstrate the likely underlying shape.

We used two previously tested methods to separate organic (CH) absorptions near 3.4 μm from carbonate (CO_3) absorptions that are found at similar wavelengths to obtain the organic-rich group of spectra (Kaplan et al. 2020; Ferrone et al. 2021); both methods resulted in similar rates of organic and carbonate identification for the Recon A dataset (Ferrone et al. 2021). The first method is linear least-squares fitting, in which we compared (unsmoothed) OVIRS spectra and laboratory spectra (at their native SNR but resampled to OVIRS spectral resolution) on a channel-by-channel basis from 2.9 to 3.6 μm to find the laboratory spectrum that best fit the shape of organic features observed in our Recon dataset. We assessed goodness of fit with a χ^2 statistic (Kaplan et al. 2020, Figure A.4). Recon A spectra that were fit by one of the organic laboratory spectra with χ^2 value < 2 were designated as organic-rich for this study, which resulted in 237 used for further analyses (e.g., in Figure 3). The full list of laboratory analog spectra used in this study is found in Tables A.1 and A.4.

The second organic detection method is an adaptation of the Kolmogorov-Smirnov goodness of fit test (Ferrone et al. 2021). We calculated the cumulative sum of OVIRS and laboratory spectra as a function of wavelength and find the maximum distance between the two curves (OVIRS and laboratory) at any wavelength (Figure A.4). The maximum distance (k) is used as our measure of goodness of fit. In Ferrone et al. (2021), Recon A spectra that were fit by one of the organic laboratory spectra with k value < 0.028 fell into the top 10% of fits, 25% of which were best fit with organic laboratory spectra. We confirm with this method that the 237 organic-rich spectra obtained from linear-least-squares fitting were also positively identified with the Kolmogorov-Smirnov method.

We tested our spectral classification methods by finding the best fitting spectral matches to noise-added laboratory spectra (Figure 1, 2, A.4). To simulate OVIRS noise, we generate random noise profiles and add them to the laboratory spectra targeting an SNR of 50, which is the nominal SNR of the OVIRS spectra in the 3.1 to 3.6 μm wavelength region and closely matches the Recon A SNR (Figure A.2). We generated 10,000 random noise profiles for each of the laboratory spectra (e.g., we created 10,000 noise-added versions of the ice tholin spectrum). We performed the linear least-squares and Kolmogorov-Smirnov fitting to determine the noise-free laboratory spectrum that best matched each of the 10,000 noise-added spectra. We tested fitting with noise-free spectra that alternately include or exclude the subject spectrum. We find that the spectral matching correctly

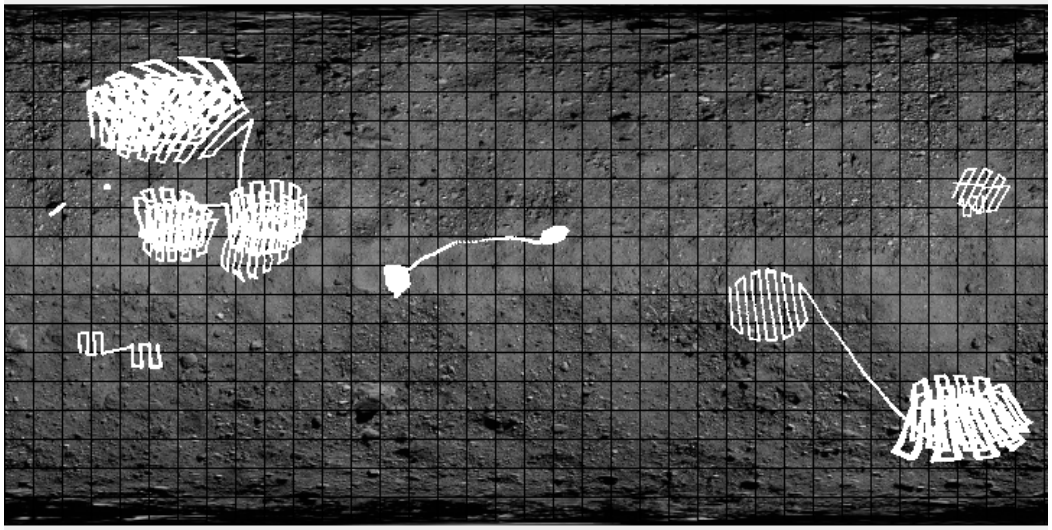

Fig. A.1. OVIRS footprints from the Recon A phase of the OSIRIS-REx mission overlaid on a Bennu basemap, which extends from -90º to 90º N and 0º to 360º E. There are 15,858 footprints shown on this map, which were analyzed for organic spectral features in this study

identifies the correct laboratory spectrum >92% of the time if the noise-added laboratory spectrum is left out of the spectral group being used for fitting (i.e., a case where we simulate having similar organics to those on Bennu in our laboratory spectra group, but not an exact match) and >99% of the time if the noise-added laboratory spectrum is kept in the spectral fitting group (i.e., a case where we simulate having an exact match for Bennu organics in our laboratory spectra) (Table A.2).

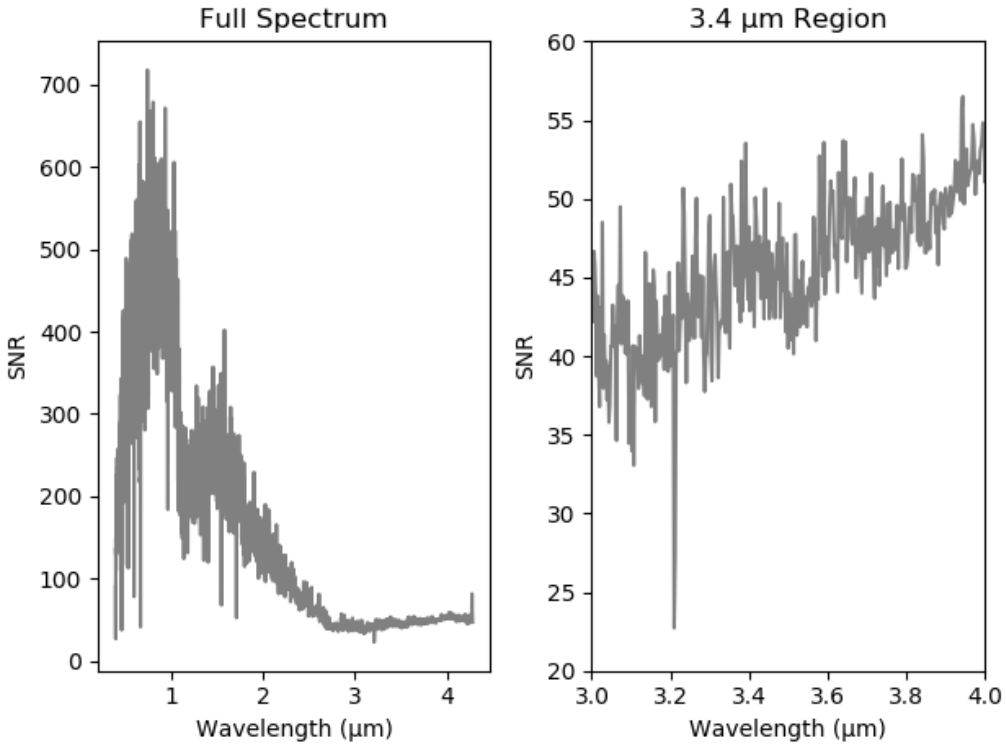

Fig. A.2. OVIRS SNR near 3.4 μm, average for Recon A.

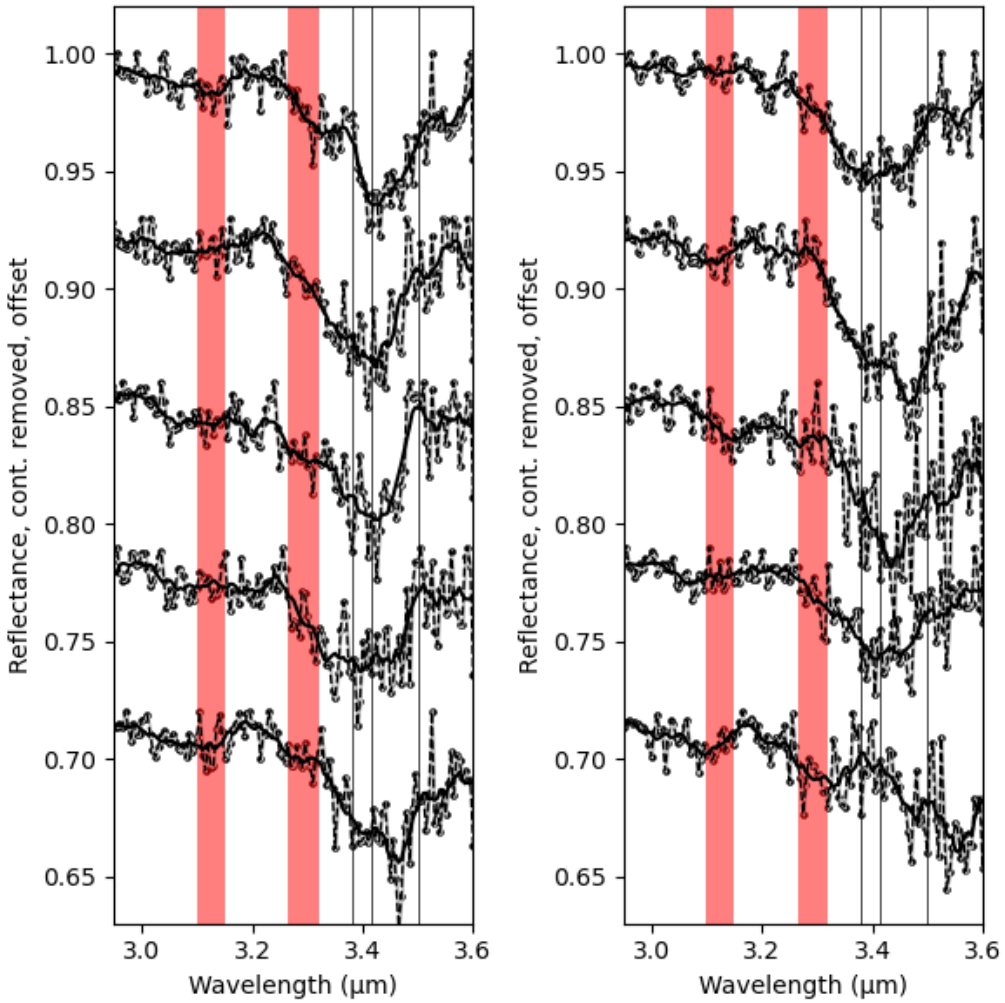

Fig. A.3. Example Bennu spectra that have a "shoulder" near 3.3 μm that may be indicative of aromatic CH. Vertical lines at 3.10, 3.275, 3.38, 3.42, and 3.50 μm indicate positions of possible absorption features.

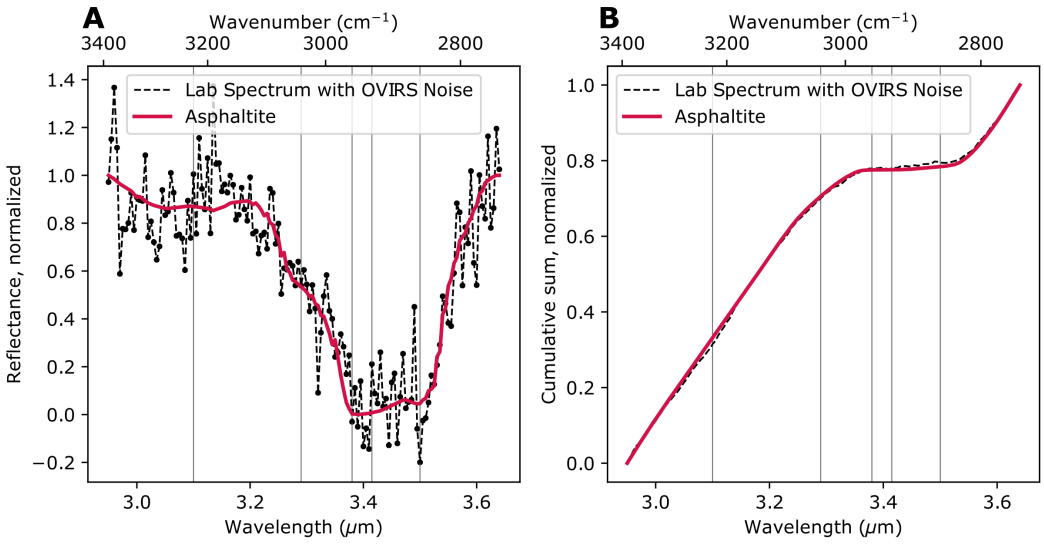

Fig. A.4. Example of the two fitting methods developed in two previous studies (Kaplan et al. 2020; Ferrone et al. 2021), a) linear least-squares fitting of normalized data and b) a Kolomogorov-Smirnov fitting method, in which we search for the maximum distance between the two curves. The black curves are laboratory data with noise added to simulate OVIRS noise and the red curves are laboratory data at their original SNR. Vertical lines at 3.10, 3.275, 3.38, 3.42, and 3.50 μm indicate positions of possible absorption features.

Table A.1. Candidate analogue organic materials

Name	Type	Source	Spectrum ID
Cold Bokkeveld IOM	Meteorite IOM	Kaplan et al. 2019	n.a.
DOM08006 IOM	Meteorite IOM	Kaplan et al. 2019	n.a.
GRO95577 IOM	Meteorite IOM	Kaplan et al. 2019	n.a.
QUE97008 IOM	Meteorite IOM	Kaplan et al. 2019	n.a.
Tag_UA_11h IOM	Meteorite IOM	Kaplan et al. 2019	n.a.
Tagish_CCL IOM	Meteorite IOM	Kaplan et al. 2019	n.a.
Tagish_DM IOM	Meteorite IOM	Kaplan et al. 2019	n.a.
Tagish_Lake IOM	Meteorite IOM	Kaplan et al. 2019	n.a.
ALH83100	Meteorite IOM	Kaplan et al. 2019	n.a.
ALH85013 IOM	Meteorite IOM	Kaplan et al. 2019	n.a.
Bells IOM	Meteorite IOM	Kaplan et al. 2019	n.a.
GRO95566 IOM	Meteorite IOM	Kaplan et al. 2019	n.a.
LEW85311 IOM	Meteorite IOM	Kaplan et al. 2019	n.a.
MET01070 IOM	Meteorite IOM	Kaplan et al. 2019	n.a.
Mighei IOM	Meteorite IOM	Kaplan et al. 2019	n.a.
Murchison IOM	Meteorite IOM	Kaplan et al. 2019	n.a.
Orgueil IOM	Meteorite IOM	Kaplan et al. 2019	n.a.
Y86720 IOM	Meteorite IOM	Kaplan et al. 2019	n.a.
K-Oxalate	Oxalate	Applin et al. 2019	n.a.
Na-Oxalate	Oxalate	Applin et al. 2019	n.a.
Ca-Oxalate	Oxalate	Applin et al. 2019	n.a.
Fe-Oxalate	Oxalate	Applin et al. 2019	n.a.
Mg-Oxalate	Oxalate	Applin et al. 2019	n.a.
NH4 citrate dibasic (with pyrrhotite)	Ammonium salt	Poch et al. 2020	NH4_citrate_dibasic_23wtpc_pyrrhotite
NH4Cl (with pyrrhotite)	Ammonium salt	Poch et al. 2020	NH4Cl_9wtpc_pyrrhotite
NH4HCO2 (with pyrrhotite)	Ammonium salt	Poch et al. 2020	NH4HCO2_17wtpc_pyrrhotite
NH4SO4 (with pyrrhotite)	Ammonium salt	Poch et al. 2020	NH4SO4_9wtpc_pyrrhotite
NH4SO4 (with pyrrhotite)	Ammonium salt	Poch et al. 2020	NH4SO4_23wtpc_pyrrhotite
Asphaltite	Complex OM	Moroz et al. 1998	n.a.
Ice Tholin	Complex OM	Khare et al., 1993	n.a.
Tyrosine	Amino acid	RELAB Spectral Library	CH-JLB-mach06
Stardust	Complex OM	Keller et al., 2006	n.a.

Samples of candidate analogue organic materials used in this study, including their source and spectrum identifier where available.

Table A.2. Spectral fitting methods applied to organic analog spectra

	% Positive Identifications for 10,000 Fits			
	All Lab Endmembers Included		Endmember to be Fit Left Out	
Type	**Group ID - Linear**	**Group ID - K-S**	**Group ID - Linear**	**Group ID - K-S**
Organics				
Meteorite IOM	99.75	99.94	92.21	88.78
Oxalate	99.46	99.31	n.a.	n.a.
Ammonium Salt	95.88	99.34	n.a.	n.a.
Asphaltite	99.53	84.76	n.a.	n.a.
Ice Tholin	99.98	87.30	n.a.	n.a.
Stardust	95.33	99.29	n.a.	n.a.
Carbonates				
Calcite	96.94	96.39	95.75	93.25
Dolomite	97.13	94.10	91.62	89.14
Magnesite	94.92	94.04	88.35	86.61

Linear least-squares (linear) and Kolmogorov-Smirnov (K-S) fitting methods were applied to laboratory endmembers with 10,000 randomly generated noise profiles simulating OVIRS noise. We fit the noise-added laboratory spectra using the noise-free laboratory endmembers listed in Tables A.1 and A.4, either including the spectrum being fit (all laboratory endmembers included) or leaving out the spectrum being fit (endmembers to be fit left out).

Table A.3. Spectral fitting methods applied to IOM spectra

	% Positive Identifications for 10,000 Fits			
IOM Name	**ID Individual - Linear**	**ID Individual - K-S**	**ID as IOM - Linear**	**ID as IOM - K-S**
Cold Bokkeveld	92.19	51.65	100	100
DOM08006	93.7	94.35	100	99.99
GRO95577	41.88	27.47	100	99.99
QUE97008	100	99.86	100	99.86
Tag_UA_11h	92.06	68.85	100	99.97
Tagish_CCL	48.08	23.52	100	99.99
Tagish_DM	99.4	95.32	100	99.98
Tagish_Lake	94.38	95.72	100	100
ALH83100	45.82	21.19	100	99.98
ALH85013	46.14	31.01	100	100
Bells	59.86	22.14	100	100
GRO95566	30.77	19.72	100	99.99
LEW85311	38.49	31.42	100	100
MET01070	36.32	35.63	100	99.99
Mighei	45.91	40.21	100	99.94
Murchison	42.2	23.05	100	99.99
Orgueil	53.87	28.43	100	100
Y86720	95.42	99.32	95.42	99.32

Results of our two spectral fitting methods linear least-squares (linear) and Kolmogorov-Smirnov (K-S) when applied to IOM spectra with 10,000 randomly generated noise profiles simulating OVIRS noise. "ID individual" refers to cases in which the noise-added laboratory spectrum is best fit with its noise-free counterpart (i.e., an exact match); "ID as IOM" refers to cases where the noise-added laboratory spectrum is best fit with another IOM spectrum (as opposed to a different laboratory endmember, e.g., a calcite), which is true nearly 100% of the time.

Table A.4. Candidate analogue carbonate materials

Name	Type	Source	Spectrum ID
CAL110 <45 um; Calcite	Calcite	RELAB Spectral Library	CA-EAC-010_M1CA10
CRB109 <45 um; Calcite	Calcite	RELAB Spectral Library	CB-EAC-009-A_LACB09A
CRB109 45-90 um; Calcite	Calcite	RELAB Spectral Library	CB-EAC-009-B_LACB09
CRB111 <45 um; Calcite	Calcite	RELAB Spectral Library	CB-EAC-011-A_LACB11A
CRB112 <45 um; Calcite	Calcite	RELAB Spectral Library	CB-EAC-012-A_LACB12A
CRB112 45-90 um; Calcite	Calcite	RELAB Spectral Library	CB-EAC-012-B_LACB12
CRB113 <45 um; Manganocalcite	Calcite	RELAB Spectral Library	CB-EAC-013-A_LACB13A
CRB113 45-90 um; Manganocalcite	Calcite	RELAB Spectral Library	CB-EAC-013-B_LACB13
CRB128 <45 um; Calcite	Calcite	RELAB Spectral Library	CB-EAC-063-A_BKR1CB063A
CRB130 <45 um; Calcite	Calcite	RELAB Spectral Library	CB-EAC-064-A_BKR1CB064A
CRB131 <45 um; Calcite	Calcite	RELAB Spectral Library	CB-EAC-065-A_BKR1CB065A
PIG004; CaCO3 Synthetic	Calcite	RELAB Spectral Library	EC-EAC-004_LAEC04
Calcite ; Calcite	Calcite	RELAB Spectral Library	GR-CMP-001_CAGR01
HYD-BLT-1a; Calcite	Calcite	RELAB Spectral Library	HM-JFM-001_C1HM01
Lane calcite 63-90	Calcite	RELAB Spectral Library	JB-JLB-550_BKR1JB550
Lane calcite 90-125	Calcite	RELAB Spectral Library	JB-JLB-551_1101S551
Lane calcite 125-180	Calcite	RELAB Spectral Library	JB-JLB-552_1101S552
Lane calcite 180-250	Calcite	RELAB Spectral Library	JB-JLB-553_1101S553
Lane calcite 250-355	Calcite	RELAB Spectral Library	JB-JLB-554_1101S554
Lane calcite 355-500	Calcite	RELAB Spectral Library	JB-JLB-555_1101S555
Mazada calcite 45-75 um	Calcite	RELAB Spectral Library	JB-JLB-E57-B_BKR1JBE57
Mazada calcite 75-90 um	Calcite	RELAB Spectral Library	JB-JLB-E57-C_BKR1JBE57C
Mazada calcite 90-125 um	Calcite	RELAB Spectral Library	JB-JLB-E57-D_BKR1JBE57D
Mazada calcite 125-250 um	Calcite	RELAB Spectral Library	JB-JLB-E57-E_BKR1JBE57E
Mazada calcite >250 um	Calcite	RELAB Spectral Library	JB-JLB-E57-F_BKR1JBE57F
Big Timber calcite <45 um	Calcite	RELAB Spectral Library	JB-JLB-E58-A_BKR1JBE58A
Big Timber calcite 45-75 um	Calcite	RELAB Spectral Library	JB-JLB-E58-B_BKR1JBE58
Big Timber calcite 75-90 um	Calcite	RELAB Spectral Library	JB-JLB-E58-C_BKR1JBE58C
Big Timber calcite 90-125 um	Calcite	RELAB Spectral Library	JB-JLB-E58-D_BKR1JBE58D
Big Timber calcite 125-250 um	Calcite	RELAB Spectral Library	JB-JLB-E58-E_BKR1JBE58E
Big Timber calcite >250 um	Calcite	RELAB Spectral Library	JB-JLB-E58-F_BKR1JBE58F
Red Calcite	Calcite	RELAB Spectral Library	PC-CMP-055_C1PC55
Calcite CaCO3	Calcite	ECOSpeclib - JPL	coarse.tir.c-3e.jpl.nicolet.spectrum
Calcite CaCO3	Calcite	ECOSpeclib - JPL	coarse.tir.calcite_1.jhu.nicolet.spectrum
Calcite CaCO3	Calcite	ECOSpeclib - JPL	coarse.tir.calcite_2.jhu.nicolet.spectrum
Calcite CaCO3	Calcite	ECOSpeclib - JPL	fine.tir.c-3d.jpl.nicolet.spectrum
Calcite CaCO3	Calcite	ECOSpeclib - JPL	fine.tir.c-3e.jpl.nicolet.spectrum
Calcite CaCO3	Calcite	ECOSpeclib - JPL	fine.tir.calcite_1.jhu.nicolet.spectrum

Table A.4. Candidate analogue carbonate materials

Calcite CaCO3	Calcite	ECOSpeclib - JPL	fine.vswir.c-3a.jpl.beckman.spectrum
Calcite CaCO3	Calcite	ECOSpeclib - JPL	medium.tir.c-3d.jpl.nicolet.spectrum
Calcite CaCO3	Calcite	ECOSpeclib - JPL	medium.tir.c-3e.jpl.nicolet.spectrum
Calcite CaCO3	Calcite	ECOSpeclib - JPL	medium.vswir.c-3a.jpl.beckman.spectrum
CRB103 <45 um; Dolomite	Dolomite	RELAB Spectral Library	CB-EAC-003-A_LACB03A
CRB103 45-90 um; Dolomite	Dolomite	RELAB Spectral Library	CB-EAC-003-B_LACB03
CRB117 <45 um; Dolomite	Dolomite	RELAB Spectral Library	CB-EAC-017-A_BKR1CB017A
Dolomite	Dolomite	RELAB Spectral Library	CC-JFM-005-B_F1CC05
Dolomite HS102	Dolomite	USGS Spectral Library Version	Dolomite_HS102.3B_NIC4bbb_RREF
Fe dolomite <125 um	Dolomite	RELAB Spectral Library	JB-JLB-779_BKR1JB779
Selasvann dolomite <45 um	Dolomite	RELAB Spectral Library	JB-JLB-E61-A_BKR1JBE61A
Selasvann dolomite 45-75 um	Dolomite	RELAB Spectral Library	JB-JLB-E61-B_BKR1JBE61
Selasvann dolomite 75-90 um	Dolomite	RELAB Spectral Library	JB-JLB-E61-C_BKR1JBE61C
Selasvann dolomite 90-125 um	Dolomite	RELAB Spectral Library	JB-JLB-E61-D_BKR1JBE61D
Selasvann dolomite 125-250 um	Dolomite	RELAB Spectral Library	JB-JLB-E61-E_BKR1JBE61E
Selasvann dolomite >250 um	Dolomite	RELAB Spectral Library	JB-JLB-E61-F_BKR1JBE61F
6521 Dolomite	Dolomite	RELAB Spectral Library	SH-SJG-077_NASH77
6523 Dolomite	Dolomite	RELAB Spectral Library	SH-SJG-078_NASH78
6528 Dolomite	Dolomite	RELAB Spectral Library	SH-SJG-079_NASH79
6529 Dolomite	Dolomite	RELAB Spectral Library	SH-SJG-080_NASH80
Dolomite CaMg(CO3)2	Dolomite	ECOSpeclib - JPL	coarse.tir.c-5a.jpl.nicolet.spectrum
Dolomite CaMg(CO3)2	Dolomite	ECOSpeclib - JPL	coarse.tir.dolomite_1.jhu.nicolet.spectrum
Dolomite CaMg(CO3)2	Dolomite	ECOSpeclib - JPL	coarse.tir.dolomite_2.jhu.nicolet.spectrum
Dolomite CaMg(CO3)2	Dolomite	ECOSpeclib - JPL	coarse.tir.dolomite_3.jhu.nicolet.spectrum
Dolomite CaMg(CO3)2	Dolomite	ECOSpeclib - JPL	fine.tir.c-5a.jpl.nicolet.spectrum
Dolomite CaMg(CO3)2	Dolomite	ECOSpeclib - JPL	fine.tir.c-5c.jpl.nicolet.spectrum
Dolomite CaMg(CO3)2	Dolomite	ECOSpeclib - JPL	medium.tir.c-5a.jpl.nicolet.spectrum
Dolomite CaMg(CO3)2	Dolomite	ECOSpeclib - JPL	medium.tir.c-5c.jpl.nicolet.spectrum
Dolomite CaMg(CO3)2	Dolomite	ECOSpeclib - JPL	solid.tir.dolomite_3.jhu.nicolet.spectrum
MGC 25-45 um; Magnesite	Magnesite	RELAB Spectral Library	BE-JFM-223_BKR1BE223
MGC 45-63 um; Magnesite	Magnesite	RELAB Spectral Library	BE-JFM-224_BKR1BE224
MGC 63-75 um; Magnesite	Magnesite	RELAB Spectral Library	BE-JFM-225_BKR1BE225
MGC 75-106 um; Magnesite	Magnesite	RELAB Spectral Library	BE-JFM-226_BKR1BE226
MGC 106-125 um; Magnesite	Magnesite	RELAB Spectral Library	BE-JFM-227_BKR1BE227
MGC 125-150 um; Magnesite	Magnesite	RELAB Spectral Library	BE-JFM-228_BKR1BE228
MGC 45-75 um; Magnesite	Magnesite	RELAB Spectral Library	BE-JFM-231_BKR1BE231
CRB106 <45 um; Magnesite	Magnesite	RELAB Spectral Library	CB-EAC-006-A_LACB06A
CRB106 45-90 um; Magnesite	Magnesite	RELAB Spectral Library	CB-EAC-006-B_LACB06
CRB208 <45 um; Hydromagnesite	Magnesite	RELAB Spectral Library	CB-EAC-028-A_LACB28A

Table A.4. Candidate analogue carbonate materials

CRB144 <45 um; Magnesite	Magnesite	RELAB Spectral Library	CB-EAC-070-A_BKR1CB070A
Brumado Bahia magnesite <45 um	Magnesite	RELAB Spectral Library	JB-JLB-946-A_BKR1JB946A
Brumado Bahia magnesite 45-75 um	Magnesite	RELAB Spectral Library	JB-JLB-946-B_BKR1JB946
Brumado Bahia magnesite 75-125 um	Magnesite	RELAB Spectral Library	JB-JLB-946-C_BKR1JB946C
Brumado Bahia magnesite <125 um	Magnesite	RELAB Spectral Library	JB-JLB-946-E_BKR1JB946E